



## Spin waves in disordered materials

P. Buczek<sup>1</sup>, S. Thomas<sup>1</sup>, A. Marmodoro<sup>2</sup>, N. Buczek<sup>3</sup>,  
X. Zubizarreta<sup>1</sup>, M. Hoffmann<sup>4</sup>, Kh. Zakeri<sup>1,5</sup>, A. Ernst<sup>1,4,\*</sup>

<sup>1</sup> Max-Planck-Institut für Mikrostrukturphysik, Weinberg 2, D-06120 Halle, Germany

<sup>2</sup> Department Chemie, Physikalische Chemie, Universität München, Butenandstraße 5-13,  
D-81377 München, Germany

<sup>3</sup> Fachhochschule Lübeck, Mönkhofer Weg 239, 23562 Lübeck, Germany

<sup>4</sup> Institut für Theoretische Physik, Johannes Kepler Universität, A 4040 Linz, Austria

<sup>5</sup> Heisenberg Spin-dynamics Group, Physikalisches Institut, Karlsruhe Institute of Technology,  
Wolfgang-Gaede-Strasse 1, D-76131 Karlsruhe, Germany

### Abstract

We present an efficient methodology to study spin waves in disordered materials. The approach is based on a Heisenberg model and enables calculations of magnon properties in spin systems with disorder of arbitrary kind and concentration of impurities. Disorder effects are taken into account within two complementary approaches. Magnons in systems with substitutional (uncorrelated) disorder can be efficiently calculated within a single-site coherent potential approximation for the Heisenberg model. The method is cheap from the computational point of view and directly applicable to systems like alloys and doped materials. It is shown that it performs exceedingly well across all concentrations and wave vectors. Another way is the direct numerical simulation of large supercells using a configurational average over possible samples. This approach is applicable to systems with arbitrary kind of disorder. The effective interaction between magnetic moments entering the Heisenberg model can be obtained from first-principles using a self-consistent Green function method within the density functional theory. Thus, our method can be viewed as an *ab-initio* approach and can be used for calculations of magnons in real materials.

## 1 Introduction

Spin waves (or magnons) are low-lying collective excitations (quasiparticles) of the electronic spin structure in a crystal lattice [1, 2, 3] and each of these excitations corresponds to a reduction in the total magnetization of the system by  $2\mu_B$ , which is manifested as a deviation of the atomic

---

\*Arthur.Ernst@jku.at

moments from their equilibrium directions [4]. Magnons are bosons, carry a fixed amount of energy  $\omega$  and a lattice momentum, and cover a very wide frequency window from gigahertz to a few hundreds of terahertz. Hence, they contribute to many observed phenomena, e.g., magnetic ordering [5], ultrafast magnetization processes [6], electronic specific heat [7], electrical and thermal conductivity [8], current induced magnetization reversal and electron spin dynamics [9]. Besides these phenomena, various coupling mechanisms with electrons and phonons in magnetocaloric materials [10] and in high-temperature superconductors [11, 12, 13, 14] can be caused by spin waves.

Magnons can be probed with various experimental methods like inelastic neutron scattering [15, 16], photons [17, 18], scanning tunneling spectroscopy (STS) [19, 20, 21, 22], spin-wave resonances [23], and spin-polarized electron energy loss spectroscopy (SPEELS) [24, 25, 26, 27, 28, 29, 30, 31, 4, 32, 33]. The most recent development in this research field was achieved for low-dimensional systems. In particular, the SPEELS and the STS techniques allow to study magnetic excitations in nanostructures such as thin films, clusters, chains and adatoms. These experiments enable direct measurements of the magnon dispersion relation, lifetime, and the group and phase velocities. Several low-dimensional systems have efficiently been studied by these methods in the last decade, for example, thin Fe, Co, Ni, Mn films on Cu(001), W(110), Pd(001), Rh(001), Ir(001) and Cu<sub>3</sub>Au(001) surfaces.

The rapid progress and success of the experiments inspired development of new theoretical approaches, which are specially designed to study magnetic excitations in complex and extended materials. One class of these methods is based on mapping of the spin system onto an effective Heisenberg Hamiltonian. This approach is utilized in many different forms like the magnetic force theorem [34], static transverse susceptibility [35, 36] and frozen magnon techniques [37]. In combination with the density functional theory, such methods do not involve adjustable parameters and are applicable to a wide range of material classes. Another way to access magnetic excitations is the direct calculation of the transverse magnetic susceptibility which poles are associated with magnons and yield their energies and life times. The magnetic susceptibility can be obtained within the linear response density functional theory [38, 39], which offers a transparent parameter free approach allowing for studying of both spin waves and Stoner excitations. This method is implemented within several numerical schemes and successfully applied to study magnons in complex bulk and low dimensional materials [40, 41, 42, 43, 44, 45, 46, 47, 48].

However, we have also take into account that the most real systems are imperfect. Structural defects, impurities, alloying can substantially modify the structural, electronic and magnetic properties of the host materials. One way to model such systems is the use of a large number of large periodic supercells where disorder is approximated by randomly generated configurations over the supercells. This method allows direct studies of arbitrary disorder, although it is very demanding with respect to the computational time. An alternative approach is the coherent potential approximation (CPA), which is a mean-field theory and designed for studies of substitutionally disordered alloys [49]. Subsequently, it was suggested to use the Green function method also to study the electronic structure of impurities and defects in various host materials [50]. In this approach the Green function of an impurity or an ensemble of atoms embedded

in a particular system can be determined in an elegant way by solving a Dyson equation, which is associated with the host material via a reference Green function. Both the supercell approach and the CPA are widely used for first-principles studies of various properties of solids. In this work, we concentrate on spin waves or magnons in disordered materials. Thereby, two main aspects will be taken into account: impact of disorder on (i) the electronic structure and magnetic interactions and, namely, on (ii) spin waves (magnons) in the disordered systems. The first matter can be efficiently treated within a standard single-site CPA approach using a self-consistent Green function method, which provides magnetic moments and exchange interaction of the disordered system from first-principles. This information can then be further used for calculations of magnons considering disorder effects either within the supercell approach or the CPA method formulated for the magnonic Green function or the transversal susceptibility. The later can be utilized either within the Heisenberg model [51, 52, 53, 54, 55, 56] or computed directly using time dependent density functional theory combined with the CPA [43].

In the current work, we present our technique to calculate spin waves in disordered materials, which is realized with both the supercell and the CPA approaches [57]. The starting point is the adiabatic spin dynamics based on the mapping of the magnetic states onto the states of the Heisenberg Hamiltonian. From the Heisenberg model, the magnetic susceptibility can be calculated either in the real space and then subsequently averaged over different disorder configurations, or it can be obtained within the CPA implemented for complex unit cells with arbitrary many types of disorder.

The paper is organized as follows. The transverse magnetic susceptibility within the adiabatic approximation is introduced in Sec. 2. Subsequently, we present our model for describing magnons in disordered systems within the real space supercell approach and the CPA method in Sec. 3 and 4, respectively. In the Sec. 5, we discuss briefly our method for calculation of the exchange parameters entering the Heisenberg Hamiltonian. The efficiency of our technique is illustrated for several examples in Secs. 3 and 4.

## 2 Transverse magnetic susceptibility

The interaction of the spins will be described in terms of the classical Heisenberg Hamiltonian. This effective Hamiltonian relates the existing spins with the magnetic exchange coefficients  $J_{ij}$  between the spins at sites  $i$  and  $j$ :

$$H = -\frac{1}{2} \sum_{ij} J_{ij} \mathbf{e}_i \cdot \mathbf{e}_j, \quad (1)$$

where  $\mathbf{e}_i$  and  $\mathbf{e}_j$  are the directions of the magnetic moments at the sites  $i$  and  $j$ , respectively. Spin waves (or magnons) are low energy excitations associated with small-amplitude precessions of moments around the main magnetization direction and can be described by the retarded transverse magnetic susceptibility  $\chi_{ij}(\omega + i0^+)$  ( $0^+$  stands for an infinitesimal positive quantity) [47]. The susceptibility gives the amplitude of the precession of the magnetic moment at the site  $i$

around its ground state direction upon applying oscillating magnetic field at the site  $j$  with frequency  $\omega$  and direction transverse to the ground state magnetization.

The susceptibility can be represented as

$$\chi = gGS, \quad (2)$$

where  $g$  is the electron g-factor, which we assume to be equal 2 in this work and  $G$  and  $S$  are matrices in the space of atomic sites.  $S$  is a diagonal matrix

$$S_{ij} = S_i \delta_{ij}, \quad (3)$$

where  $S_i$  is the spin moment at the site  $i$  and  $G$  is the *magnon spin propagator*

$$G(z) = G_0(z) + G_0(z)gSTG, \quad (4)$$

$$G_0(z) = \mathbb{1}z^{-1}, \quad (5)$$

where  $z$  stands for the complex frequency,  $\mathbb{1}$  is the unit matrix,  $G_0$  is the *free spin propagator* and the *torque matrix*  $T$  is defined as

$$(ST)_{ij} = S_j^{-1} \delta_{ij} \sum_l J_{il} - S_j^{-1} J_{ij}. \quad (6)$$

Eq. (5) can be formally solved by the matrix inversion

$$G^{-1} = G_0^{-1} - gST, \quad (7)$$

which allows to compute the susceptibility for any frequency using Eq. (2).

In principle, the formula (2) above would be enough to calculate the loss from the susceptibility matrix  $\chi$  [47],

$$\mathcal{L}\chi(\omega + i0^+) = \frac{1}{2i} \left( \chi(\omega + i0^+) - \chi(\omega + i0^+)^\dagger \right), \quad (8)$$

associated with the spectral density of the excitations at the given energy  $\omega$  and the corresponding eigenvectors give the spatial form of the excitations. The main target is the calculation of the average susceptibility and the corresponding loss in a disordered supercell. This can be achieved by averaging the susceptibility  $\chi(\omega + i0^+)$  over a larger amount of differently occupied supercells (so called configurations) or by solving corresponding CPA equations.

### 3 Numerical averaging of magnons in real space

The transverse magnetic susceptibility can be directly calculated in real space for a supercell  $\mathbf{R}^{\text{sc}}$ , which is a subdivision of an infinite crystal (see Fig. 1). Each position  $i$  of the crystal is occupied by atoms of types  $\alpha, \beta, \dots$  with some given probabilities  $c_i^\alpha, c_i^\beta$ , etc. We introduce

the occupation function  $p^\alpha(\mathbf{r}_i)$ , which is 1 if the site  $i$  is occupied by the atom of the type  $\alpha$  and 0 otherwise. In addition, we assume that the occupation of one site does not influence the occupation of the other sites, i.e., the disorder is uncorrelated. The atomic occupation in the supercell  $\mathbf{R}^{\text{sc}}$  is chosen with respect to the probabilities  $c_i^A$ . The susceptibility of the disordered system  $\langle \chi \rangle$  is then obtained by averaging over many such configurations (typically between 100 and 1000 created using pseudorandom numbers).

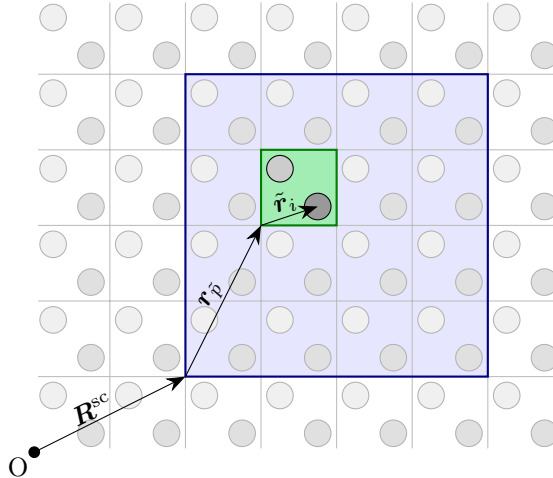


Figure 1: Definition of coordinates. The simulation domain is a supercell (blue) with its origin being located at  $\mathbf{R}^{\text{sc}}$ . It consists of unit cells (green) at  $\mathbf{r}_{\tilde{p}}$  with respect to the origin of the supercell and the unit cells may contain several basis atoms (circles) at  $\tilde{\mathbf{r}}_i$ .

A general extension to this algorithm is the introduction of an additional subdivision of the supercell  $\mathbf{R}^{\text{sc}}$  into basis sites  $\alpha$  in a cell  $\tilde{p}$  (see Fig. 1) by splitting the vectors as

$$\mathbf{r}_i = \mathbf{R}^{\text{sc}} + \mathbf{r}_{\tilde{p}} + \tilde{\mathbf{r}}_i. \quad (9)$$

Afterwards, it is possible to fold the supercell back to the original unit cell by application of a Fourier transformation

$$\langle \chi_{ij}(\mathbf{q}) \rangle = \sum_{\tilde{p}} \sum_{\tilde{t}} e^{i\mathbf{q} \cdot \mathbf{r}_{\tilde{p}}} e^{-i\mathbf{q} \cdot \mathbf{r}_{\tilde{t}}} \langle \chi_{(\tilde{p},i),(\tilde{t},j)}(\mathbf{q}) \rangle, \quad (10)$$

where  $\mathbf{q}$  is the wave vector from the first Brillouin zone and the sums run over all unit cells  $\tilde{p}$  and  $\tilde{t}$ .

### 3.1 Generation of random structures

The generation of random structures, i.e., different occupations of the simulated supercells, is a critical part in the calculation of the susceptibility of disordered systems and plays an important role in the success of the method. The main goal of the following algorithms is to resemble real physical structures as closely as possible.

Especially for surface structures, it is important to find reasonable methods, because the growth

process will impact the resulting structures: Fig. 2a shows 7 monolayers of Co deposited on Cu(001), which yields a rugged surface structure with several different thicknesses and plateaus with diameters of a few nanometers. To reduce the impact of this disorder, the sample was annealed at 370 K to obtain a much smoother surface (cf. Fig. 2b) [58]. However, since films with less than 6 monolayers of Co on Cu(100) suffer from diffusion of Cu to the surface, while annealing [58], the rugged structures are a necessary target for the structure generation algorithm. For the simulation of smooth annealed surfaces, an algorithm capable of avoiding a surplus amount of point defects would be favorable.

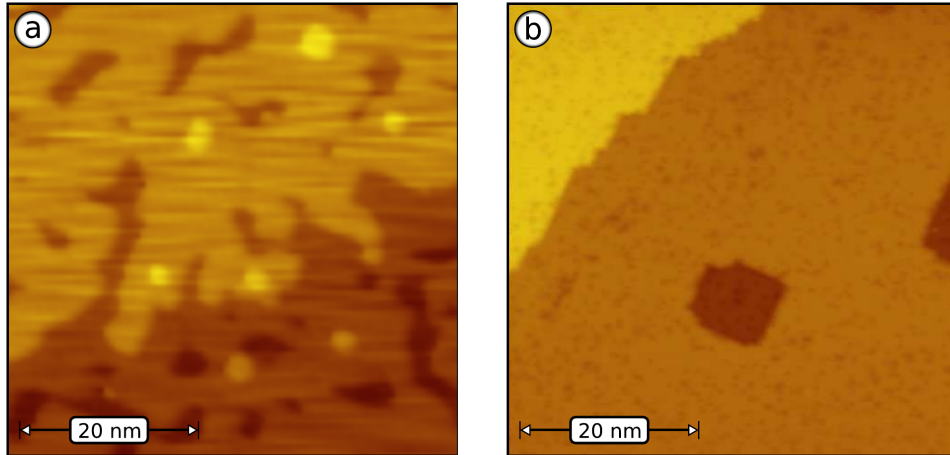


Figure 2: Surface tunneling microscopy (STM) pictures of (a) as-deposited 7ML Co/Cu(100), (b) Co/Cu(100) after annealing at 370 K. Different colors denote different surface heights [58].

In the following, three major algorithms are presented, which were used for the creation of random structures. They are focused on performance and tunability of the resulting outputs. Because of their versatility and good comparison with the shown experimental surfaces, they were chosen over more complex algorithms, like kinetic Monte Carlo approaches.

### 3.1.1 Direct random structure generation and Fisher-Yates-Shuffle

The most straightforward approach to create random structures is the use of standard pseudo-random numbers (PRN). A given setup and equally distributed PRNs in the right-open interval  $[0..1)$  – the output of most standard PRN generators – offer two basic ways to create the desired random distribution of atoms.

The first method is the direct use of the random numbers by dividing the interval according to the probabilities of each species at a given site. For example, a probability of 40 % for species A and 60 % for species B would result in species A for all random numbers  $p < 0.4$  and species B, otherwise. An important caveat of this method is the possibility of an unbalanced system, where the actual final composition does not meet the desired probabilities (if at all possible due to the limited amount of lattice positions in the supercell). In this case, an additional rebalancing step might be necessary.

The second method is the use of the Fisher-Yates-Shuffle [59]:

---

**Algorithm 1** Fisher-Yates-Shuffle

---

**Require:**  $a(1 : n)$  contains desired composition

```
for  $i = n$  downto 2 do
   $j \leftarrow$  random integer  $1 \leq j \leq i$ 
  swap  $a(i) \leftrightarrow a(j)$ 
end for
```

---

For a given site in the original unit cell, a list of all corresponding positions in the supercell is created and filled with the desired composition of species in an arbitrary order. Applying the above example to a system with 25 sites would result in a list filled with 10 entries of A and 15 entries of B. Then, the Fisher-Yates-Shuffle will create a completely random permutation of this composition, which can then be used for further calculations.

Nevertheless, both methods can produce unphysical or undesired results. For example, the calculation of the system 3ML Co/Cu(001) where 50% of Co atoms from the 3th layer are moved to the 4th layer will most likely produce floating atoms or holes (see Fig. 3).

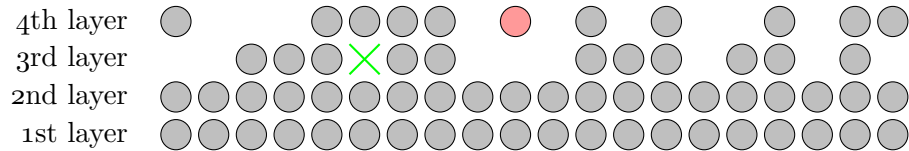


Figure 3: Sideview of a possible random configuration for 3ML Co/Cu(001), where 50% of the atoms from the 3th layer are moved to the 4th layer. Possibly undesired floating atoms (red) and holes (green) were created.

### 3.1.2 Perlin noise method

This method is based on the popular Perlin noise [60, 61], which is commonly used for procedural creation of textures in computer graphics. The idea of this approach is to model the surface in terms of a smooth noise function. Some form of downsampling is applied to create a closed hilly surface which can be used in susceptibility calculations.

In order to create Perlin noise on a grid (in this case, the supercell), a second grid with a lower resolution is generated and its vertices are populated with random gradient vectors. Then, for every point in the supercell, i.e., the high-resolution grid, the contributions from the nearest gradient vectors are weighted to get a smooth noise function. In the 1-dimensional case (see Fig. 4), the gradients from the vertices to the left and to the right are used and the resulting linear functions are interpolated. In the 2-dimensional case, the interpolation would be calculated from the 4 vertices of the circumscribing rectangle.

In Fig. 4, it becomes apparent that this definition of Perlin noise results in the value "zero" at each of the low-resolution grid's vertices. For that reason, an additional contribution of cubically interpolated regular noise, which is also defined at the vertices of the low-resolution grid, was added to the Perlin noise. The generation of the final structure from the Perlin noise is then achieved with the help of a level-set method (see Fig. 5). In this method, one or more thresholds

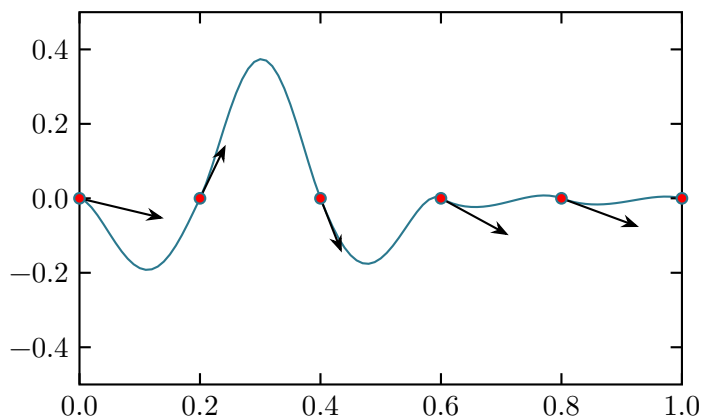


Figure 4: Example for 1-dimensional Perlin noise (blue line). The low-resolution grid is defined at the red points and the gradient vectors are represented by arrows.

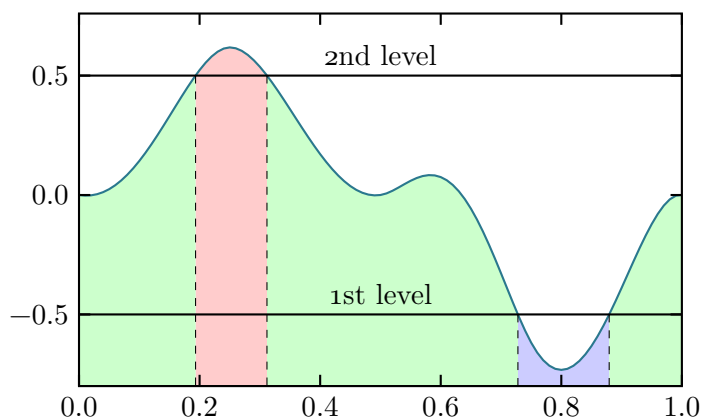


Figure 5: Level-set method with 2 levels at 0.5 and  $-0.5$  applied to 1-dimensional Perlin noise. The blue area is below the 1th level, the green areas between both levels and the red area is above the 2th level.

are defined and compared to the noise function at every position in the grid. The example in the figure can be interpreted as a 1-dimensional surface. Positions, where the noise function is less than the 1th level, would get assigned no atoms, positions with a value between the two levels get assigned one atom and positions with a value above the 2th level get assigned two atoms.

This method has the same problems concerning stoichiometry as the purely random distribution of atoms. To get closer to the desired composition, the thresholds of the level set method can be adapted to fit the needs of the calculation. Another problem is the fact that this method can only be defined on a rectangular grid. As a result, the application of Perlin noise to a non-rectangular supercell, which is needed for calculations of, e.g., a hexagonal surface represented by rhombic unit cells, would result in a distorted grid with a strong anisotropy. In particular, one diagonal of the unit cell is longer than the other resulting in a structure, which is stretched along the longer diagonal. A possible solution is provided by simplex noise [62], a later invention of [62], which is defined on a triangular grid.

### 3.1.3 Random structures from Voronoi tessellation

The third possible method is based on a Voronoi tessellation of the supercell.

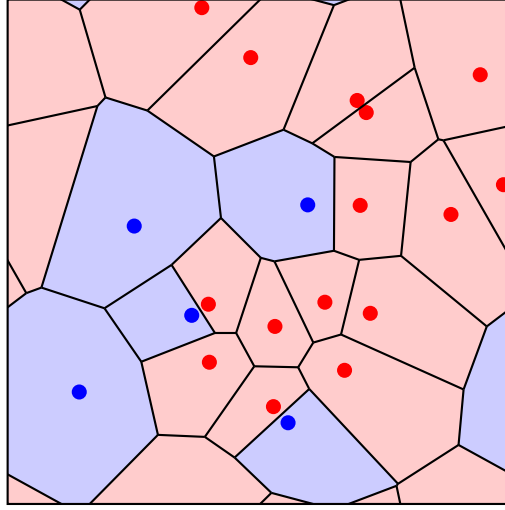


Figure 6: Example of 2-dimensional Voronoi tessellation with 2 different species (red and blue). The dots represent the initial points  $\mathbf{P}_k$ . The corresponding Voronoi regions  $R_k$  (separated by black lines) get the same lighter color (same species) as the  $\mathbf{P}_k$  inside that region.

To create the desired distribution of atoms in the supercell, some points  $\mathbf{P}_k$  (which get marked with a species label) are put into the supercell and the Voronoi tessellation (with cyclical boundary conditions) is computed. The Voronoi regions  $R_k$  get the same species label as the corresponding points (see Fig. 6). In the next step, the atoms in the supercell get assigned the appropriate species, determined by the species label of the Voronoi region at the corresponding position (see Fig. 7).

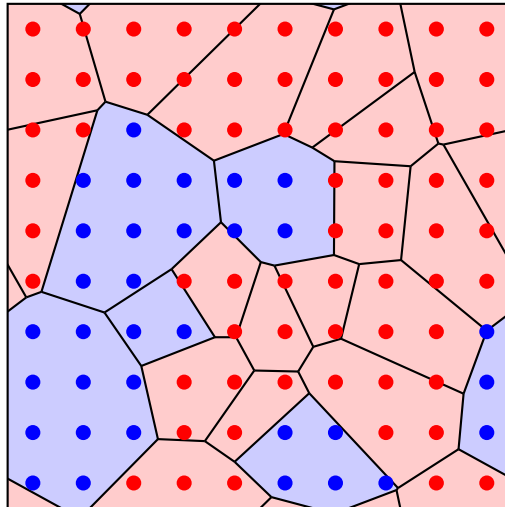


Figure 7: Resulting distribution of atom species from Voronoi tessellation in Fig. 6. All other points (basis sites of the supercell) are now assigned with the respective color of their region (reddish or bluish).

Similar to the other methods, additional steps are needed to get the desired stoichiometry. This can be achieved using a weighted Voronoi tessellation and optimizing the weights  $w_k$  towards the desired composition:

$$R_k = \{ \mathbf{x} \in \mathbb{R}^n \mid d(\mathbf{x}, k) \leq d(\mathbf{x}, j), \forall j \neq k \}, \quad (11)$$

$$d(\mathbf{x}, k) = w_k \cdot \|\mathbf{x} - \mathbf{P}_k\|_2. \quad (12)$$

Due to the fact that the Voronoi regions are defined by the points in the supercell, there are no limitations to the shape of the supercell. Additionally, the size of the generated structures (i.e., clusters of similar atoms) can be tuned by the composition and amount of the initial points  $\mathbf{P}_k$ .

### 3.1.4 Application of generators

From the properties of the three methods, it is straightforward to determine which method should be used for a given system: The 2-dimensional systems, i.e., such as 7ML Co/Cu(001) or similar, could be created with the Perlin method. Depending on the size of the surface's features, a varying resolution of the coarse grid can be used. While the annealed system can be obtained from the algorithm as described, the unannealed system could be generated with a high-resolution "coarse" grid to effectively switch of its smoothing capability. On the other hand, a purely random composition might produce acceptable results for the unannealed structure, but this was not used in actual calculations.

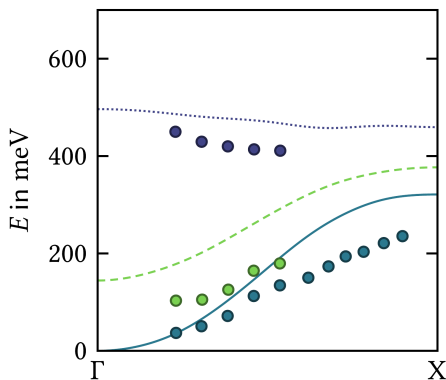


Figure 8: Magnons in the ordered 3ML Co/Cu(001) calculated using the Heisenberg model (lines) and compared with the results of the SPEELS measurements (dots).

As a reference, we calculated spin waves obtained for an ordered 3ML Co film on the Cu(001) surface (assuming ideal growth conditions) and compared with SPEELS measurements performed by Kh. Zakeri *et al.* (Fig. 8). Indeed, the theory can not reproduce correctly the acoustic mode in higher wave vectors, although for lower energies and small wave vectors the agreement is rather well. The first optical branches are substantially overestimated by the theory for all wave vectors, especially for the lowest optical mode. Hence, we applied the Perlin method to create more realistic supercells and calculated again the spin waves in 3ML Co/Cu(001) for atomic configurations like those shown in Fig. 3. This structure was elucidated from the recent STM measurements by Balashov *et al.* [58]. The calculated magnetic susceptibility within this

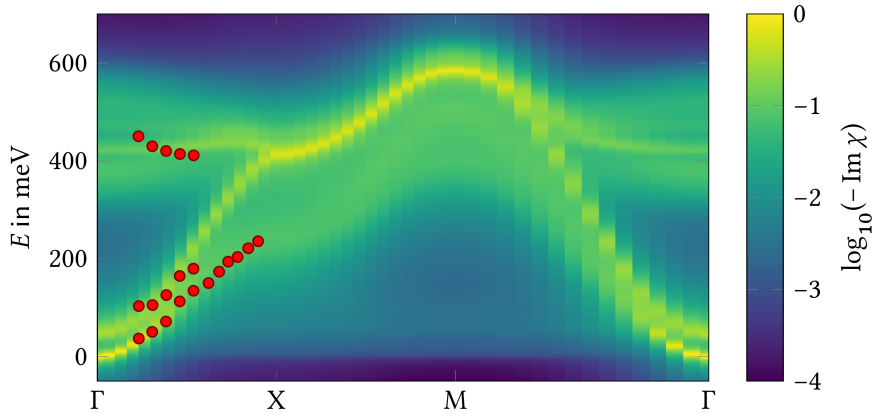


Figure 9: Calculated magnons in 3ML Co/Cu(001) shown as contour plot together with the results of the SPEELS measurements (dots). Direct numerical averaging and supercells created with the Perlin method and the structural model shown in Fig. 3 were used.

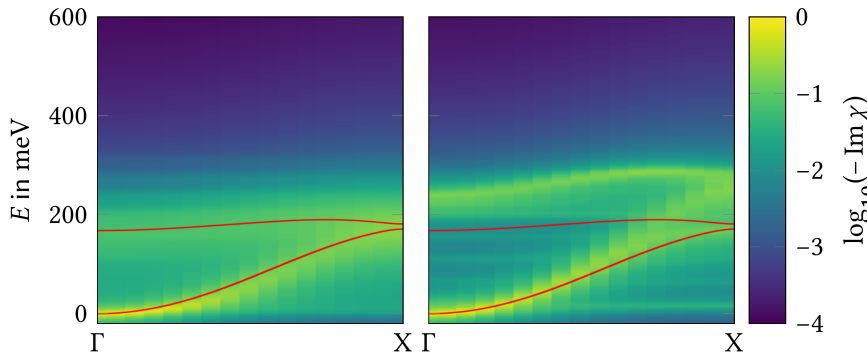


Figure 10: Spin-wave spectra of 1ML Fe on Pd with an actual composition of  $(\text{Fe}_{0.7}\text{Pd}_{0.3} | \text{Fe}_{0.3}\text{Pd}_{0.7})$  for the surface and first subsurface layer, respectively. The left panel shows the purely random structure, the right panel shows a structure with islands. Continuous red lines represent the VCA calculations for this alloy.

structural model is in very good agreement with experimental results (see Fig. 9).

However, the spin wave energies can be also significantly modified by the presence of islands, which could arise during growth processes. We studied magnons in the disordered system of 1ML of Fe on the Pd(001) surface. The growth of Fe on a Pd substrate depends strongly on the deposition temperature [63]. Varying the deposition temperature one obtains various alloy configurations in the surface and the first subsurface layers. At certain conditions Fe and Pd atoms are not mixed randomly but forming small islands within the surface double layer. Such clustering increases magnon energies for larger wave vectors (see Fig. 10). For comparison, we calculated also spin waves using a so called virtual crystal approximation (VCA), which reproduces rather well results for the purely random structure (red lines in Fig. 10).

For 3-dimensional systems, the most important property is the short-range order of the system. If the atoms of the different species are randomly distributed, a purely random generation is

preferred, and if a clustering of similar atoms is observable, the Voronoi tessellation is the method of choice. In the latter case, a 3-dimensional variant of the Perlin method would also be possible, but this was not implemented because of the limitations apparent from the 2-dimensional version.

## 4 CPA for Heisenberg model

Now we consider our implementation of the CPA Heisenberg model. Therein, we have followed the formalism suggested by Matsubara [51] and Yonezawa [64]. This approach does not take into account off-diagonal disorder, which can be incorporated within the local Blackman, Esterling, and Berk (BEB) method [65]. Several realizations of the Heisenberg model within the BEB approach were suggested over the last fifty years [52, 53, 56]. Although the implementations of the method by different authors differ in details, the foundation of all works on the Heisenberg-CPA are similar. Our implementation based on the derivation by Matsubara und Yonezawa is generalized for the case of complex unit cells, arbitrary number of atomic species forming the disordered system, and arbitrary dimensionality.

The coherent potential approximation for the transverse magnetic susceptibility of the Heisenberg Hamiltonian is constructed as follows. We define the *species resolved Fourier transformation of the susceptibility*

$$\chi_{ij}^{\alpha\beta}(\mathbf{q}, \mathbf{q}') = \sum_{\mathbf{R}\mathbf{R}'} p^{\alpha i}(\mathbf{R}) e^{-i\mathbf{q}\cdot\mathbf{R}} \chi(\mathbf{R} + \tilde{\mathbf{r}}_i, \mathbf{R}' + \tilde{\mathbf{r}}_j) p^{\beta j}(\mathbf{R}') e^{i\mathbf{q}'\cdot\mathbf{R}'}, \quad (13)$$

where the notation of vectors is similar as in Fig. 1 but in contrast to Eq. (10) we consider only unit cells  $\mathbf{R}$ . The occupation function defined in Sec. 3 is written as  $p^{\alpha i}(\mathbf{R}) := p^{\alpha}(\mathbf{R} + \tilde{\mathbf{r}}_i)$ . Eq. (13) allows to compute the Fourier transform of the full susceptibility as

$$\chi_{ij}(\mathbf{q}, \mathbf{q}') = \sum_{\alpha\beta} \chi_{ij}^{\alpha\beta}(\mathbf{q}, \mathbf{q}'). \quad (14)$$

The susceptibility  $\chi(z, \mathbf{q}, \mathbf{q}')$  corresponds to a single random configuration of the atoms constituting the alloy.

Following Eq. (5), the susceptibility in the real space can be developed in a formal series

$$\begin{aligned} \chi(z) = & G_0 g S + G_0 g S T G_0 g S \\ & + G_0 g S T G_0 g S T G_0 g S + \dots, \end{aligned} \quad (15)$$

where the  $ST$  product is given by Eq. (6).

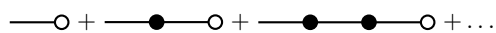


Figure 11: Expansion of the  $\chi_{ij}^{\alpha\beta}(z, \mathbf{q}, \mathbf{q}')$  susceptibility.

The Fourier transformation  $\chi_{ij}^{\alpha\beta}(z, \mathbf{q}, \mathbf{q}')$  can be computed term-by-term upon a series of tedious algebraic manipulations and has the diagrammatic representation depicted in Fig. 11. The

diagram consists of three elements listed below. Each of the elements is a matrix in a space of composite indices involving basis sites and atomic species. The following notation is used  $(i) \equiv i\alpha$ ,  $(j) \equiv j\beta$ ,  $(l) \equiv l\gamma$ ,  $(m) \equiv m\mu$ , etc. Furthermore, in this index space the Einstein summation convention is used. The elements are

1.  $\mathcal{T}$ -matrix denoted with filled circle ( $\bullet$ )

$$\mathcal{T}_{ij}^{\alpha\beta}(\mathbf{q}, \mathbf{q}') = \rho^{(l)}(\mathbf{q} - \mathbf{q}') \tau_{(i)(j)}^{(l)}(\mathbf{q}, \mathbf{q}'), \quad (16)$$

where

$$\tau_{(i)(j)}^{(l)}(\mathbf{q}, \mathbf{q}') \equiv gS_{\beta}^{-1} \left( J_{jl}^{\beta\gamma}(\mathbf{q} - \mathbf{q}') \delta_{(i)(j)} - J_{lj}^{\gamma\beta}(\mathbf{q}') \delta_{(i)(l)} \right), \quad (17)$$

$$\rho^{\alpha i}(\mathbf{q}) \equiv \sum_{\mathbf{R}} p^{\alpha i}(\mathbf{R}) e^{-i\mathbf{q}\cdot\mathbf{R}}, \quad (18)$$

$$J_{ij}^{\alpha\beta}(\mathbf{q}) \equiv \sum_{\mathbf{R}} J_{ij}^{\alpha\beta}(\mathbf{R}) e^{-i\mathbf{q}\cdot\mathbf{R}}. \quad (19)$$

The two latter quantities are lattice Fourier transformations of the occupation function and the exchange parameters, respectively.

2.  $\mathcal{S}$ -matrix denoted with open circle ( $\circ$ )

$$\mathcal{S}_{(i)(j)}(\mathbf{q}, \mathbf{q}') = \rho^{(l)}(\mathbf{q} - \mathbf{q}') \sigma_{(i)(j)}^{(l)}, \quad (20)$$

$$\sigma_{(i)(j)}^{(l)} \equiv g\delta_{(i)(j)}\delta_{(i)(l)}S_{(l)}. \quad (21)$$

3. Propagator of uncoupled magnetic moments ( $\text{---}$ )

$$\Gamma_{(i)(j)}(z) = z^{-1}\delta_{(i)(j)}. \quad (22)$$

This matrix does not depend on the momentum but introduces the frequency dependence into the equations.

The rules for evaluating the diagrams are as follows:

1. The matrices in the  $(i)(j)$  space brought together in a diagram undergo the matrix multiplication in this space.
2. Every internal free propagator line is associated with an integration over a Brillouin zone, denoted as

$$\frac{1}{\Omega_{\text{BZ}}} \int_{\mathbf{q} \in \Omega_{\text{BZ}}} f(\mathbf{q}) \, d\mathbf{q} \equiv \int_{\mathbf{q}} f(\mathbf{q}), \quad (23)$$

in order to simplify the notation.

For instance, the second term, i.e. including the product of two random variables  $\rho^{(i)}(\mathbf{q})$ , in the

expansion presented in Fig. 11 is explicitly written as

$$\chi_{ij}^{\alpha\beta}(z, \mathbf{q}, \mathbf{q}') = z^{-2} \int_{\mathbf{q}_1} \mathcal{T}_{(i)(m_1)}(\mathbf{q}, \mathbf{q}_1) \mathcal{S}_{(m_1)(j)}(\mathbf{q}_1, \mathbf{q}'),$$

(2<sup>nd</sup> order) (24)

$$= z^{-2} \rho^{(l_1)}(\mathbf{q} - \mathbf{q}_1) \tau_{(i)(m)}^{(l_1)}(\mathbf{q}, \mathbf{q}_1) \rho^{(l_2)}(\mathbf{q}_1 - \mathbf{q}') \sigma_{(m)(j)}^{(l_2)}.$$
(25)

(Note the Einstein convention for the indices  $(l_1)$ ,  $(l_2)$ , and  $(m)$ .)

In the next step, our goal is to compute the averaged susceptibility. Upon the averaging, the translational symmetry of the system is restored and the susceptibility depends only on one wave-vector variable

$$\langle \chi_{ij}^{\alpha\beta}(z, \mathbf{q}, \mathbf{q}') \rangle \equiv \langle \chi_{ij}^{\alpha\beta}(z, \mathbf{q}) \rangle \Omega_{\text{BZ}} \delta(\mathbf{q} - \mathbf{q}').$$
(26)

In what follows, we will construct the coherent potential approximation for  $\langle \chi_{ij}^{\alpha\beta}(z, \mathbf{q}) \rangle$ . We attempt to average every term of the expansion presented in Fig. 11 separately and following Yonezawa [64], we resort to the so called cumulant expansion. As example, let us consider again the 2<sup>nd</sup> order term given in Eq. (25)

$$\langle \chi_{ij}^{\alpha\beta}(z, \mathbf{q}, \mathbf{q}') \rangle = z^{-2} \tau_{(i)(m)}^{(l_1)}(\mathbf{q}, \mathbf{q}_1) \sigma_{(m)(j)}^{(l_2)} \langle \rho^{(l_1)}(\mathbf{q} - \mathbf{q}_1) \rho^{(l_2)}(\mathbf{q}_1 - \mathbf{q}') \rangle.$$
(27)

We note that only the  $\rho$  functions contain random variables  $p$  and require averaging. The cumulant expansion of the product reads

$$\langle \rho^{(l_1)}(\mathbf{k}_1) \rho^{(l_2)}(\mathbf{k}_2) \rangle = \mathcal{C}_{(l_1)(l_2)}^2(\mathbf{k}_1, \mathbf{k}_2) + \mathcal{C}_{(l_1)}^1(\mathbf{k}_1) \mathcal{C}_{(l_2)}^1(\mathbf{k}_2),$$
(28)

where  $\mathcal{C}^n$  stands for the multivariate cumulant of order  $n$ . In the case of the uncorrelated disorder

$$\mathcal{C}_{(l_1)(l_2)\dots(l_n)}^n(\mathbf{k}_1, \mathbf{k}_2, \dots, \mathbf{k}_n) = \mathcal{P}_{(l_1)(l_2)\dots(l_n)}^n(\mathbf{c}) \Omega_{\text{BZ}} \delta(\mathbf{k}_1 + \mathbf{k}_2 + \dots + \mathbf{k}_n),$$
(29)

where  $\mathbf{c}$  is the concentration matrix  $c_{i\alpha}$ . The weight functions  $\mathcal{P}$  in the uncorrelated case are non-zero only if all indices correspond to the same basis site. They do not have any straightforward analytic representation but the first two read

$$\mathcal{P}_{i\alpha}^1(\mathbf{c}) = c_{i\alpha},$$
(30)

$$\mathcal{P}_{i\alpha j\beta}^2(\mathbf{c}) = \delta_{ij} (\delta_{\alpha\beta} c_{i\alpha} - c_{i\alpha} c_{i\beta}).$$
(31)

From the momentum dependence of the cumulants follows, as expected from Eq. (26), that the averaged susceptibility is diagonal in the momentum arguments and, thus, proportional to  $\Omega_{\text{BZ}} \delta(\mathbf{q} - \mathbf{q}')$ .

Examples of the cumulant expansion for the second and fourth order terms are presented in Fig. 12. The coherent potential approximation neglects the terms involving multiple ‘‘crossed’’ cumulants. The lowest order term of this type appears in the 4th order average and is marked



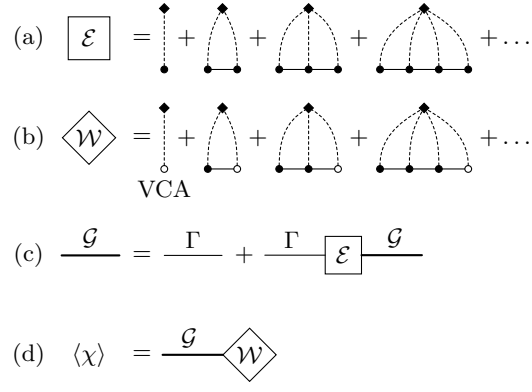


Figure 13: The diagrammatic representation of the Dyson equation for the CPA susceptibility: expansions of the CPA self-energy (a) and the magnetic weight (b) given by Eqs. (33) and (34) respectively, (c) the Dyson equation (32), and (d) the final expression for the averaged susceptibility corresponding to Eq. (35). Restricting the series in (a) and (b) to the first terms only yields the virtual crystal approximation.

The final expression for the averaged susceptibility involves the matrix product of the effective propagator and the weight correction

$$\langle \chi(z, \mathbf{q}) \rangle = \mathcal{G}(z, \mathbf{q}) \mathcal{W}(z, \mathbf{q}). \quad (35)$$

The expansion presented above is depicted in terms of diagrams in Fig. 13. The calculation process involves self-consistency, as the effective medium propagator  $\mathcal{G}$  is found using the self-energy  $\mathcal{E}$ , which in turn involves the propagator.

The series given by Eqs. (33) and (34) do not converge term-by-term. Furthermore, it is computationally unfeasible to work directly in the reciprocal space. Below, we transform the corresponding quantities to the real space representation, where we sum over the series. For simplicity the frequency arguments are suppressed

$$\mathcal{E}(\mathbf{q}) = \mathcal{E}(\mathbf{q}, \mathbf{q}) \equiv \sum_{\mathbf{R}\mathbf{R}'} \mathbf{e}^{-\mathbf{q}\cdot(\mathbf{R}-\mathbf{R}')} \mathcal{E}(\mathbf{R}, \mathbf{R}'), \quad (36)$$

$$\mathcal{W}(\mathbf{q}) \equiv \sum_{\mathbf{R}} \mathbf{e}^{-\mathbf{q}\cdot\mathbf{R}} \mathcal{W}(\mathbf{R}), \quad (37)$$

$$\mathcal{E}(\mathbf{R}, \mathbf{R}') = \sum_{i\alpha} c_{i\alpha} \sum_{\mathbf{R}_1} \hat{\mathcal{E}}^{i\alpha}(\mathbf{R}, \mathbf{R}_1) \tau^{i\alpha}(\mathbf{R}_1, \mathbf{R}'), \quad (38)$$

$$\mathcal{W}(\mathbf{R}) = \sum_{i\alpha} c_{i\alpha} \hat{\mathcal{E}}^{i\alpha}(\mathbf{R}, \mathbf{0}) \sigma^{\alpha i}. \quad (39)$$

The *partial self-energies*  $\bar{\mathcal{E}}$  are determined as follows

$$\bar{\mathcal{E}}^i(\mathbf{R}, \mathbf{R}') = \sum_{\alpha \in I_i} \sum_{\mathbf{R}_1} c_{i\alpha} \hat{\mathcal{E}}^{i\alpha}(\mathbf{R}, \mathbf{R}_1) \mathcal{M}^{i\alpha}(\mathbf{R}_1, \mathbf{R}'), \quad (40)$$

where  $I_i$  denotes the set of impurity types present on site  $i$ . The terms off-diagonal in the sites'

space are zero in the case of uncorrelated disorder. In what follows, we will work with matrices in a space of extended composite indices including both the composite index ( $i$ ) as well as the lattice vector  $\mathbf{R}$ , i.e.  $(\alpha i \mathbf{R})$ . It is sufficient to consider only finite clusters of lattice vectors corresponding to the range of the exchange parameters  $J(\mathbf{R})$ . Using the concept of the effective interaction of Yonezawa, the summation of the cumulant series yields

$$c_{i\alpha} \hat{\mathcal{E}}^{i\alpha} = \mathcal{P}_{i\alpha}^1 \mathbb{1} + \mathcal{P}_{i\beta, i\alpha}^2 \mathcal{M}^{i\beta} + \mathcal{P}_{i\gamma, i\beta, i\alpha}^3 \mathcal{M}^{i\gamma} \mathcal{M}^{i\beta} + \dots, \quad (41)$$

$$\hat{\mathcal{E}}^{i\alpha} = (\mathbb{1} - (\mathcal{M}^{i\alpha} - \bar{\mathcal{E}}^i))^{-1}, \quad (42)$$

where the  $\mathcal{M}$  matrices are defined in the reciprocal space by

$$\mathcal{M}_{(i)(j)}^{(l)}(\mathbf{q}, \mathbf{q}') = \tau_{(i)(m)}^{(l)}(\mathbf{q}, \mathbf{q}') \mathcal{G}_{(m)(j)}(\mathbf{q}'), \quad (43)$$

and in the real space consist of two parts

$$\begin{aligned} \mathcal{M}_{(i)(j)}^{(l)}(\mathbf{R}, \mathbf{R}') &= g S_\alpha^{-1} J_{il}^{\alpha\gamma}(\mathbf{R}) \mathcal{G}_{(i)(j)}(\mathbf{R} - \mathbf{R}') \\ &\quad - \sum_{\mathbf{R}_1} \left[ g S_\mu^{-1} J_{lm}^{\gamma\mu}(\mathbf{R}_1) \mathcal{G}_{(m)(j)}(\mathbf{R}_1 - \mathbf{R}') \delta_{(i)(l)} \delta_{\mathbf{R}\mathbf{0}} \right]. \end{aligned} \quad (44)$$

The equations above can be directly implemented on a computer in order to find  $\langle \chi \rangle$  and we conclude this section with several remarks concerning our numerical scheme. The convergence of the CPA self-consistency loop requires a suitable mixing of quantities from previous iterations and we resorted to the Broyden method in order to achieve it. Furthermore, the self-consistent loop does not converge for complex energies with small imaginary parts. To remedy the latter difficulty, we resorted to the nearly real axis method [47]. The self-consistent quantities were converged in a suitable distance away from the real axis and subsequently the self-energy  $\hat{\mathcal{E}}(z)$  was analytically continued towards the real energies in order to recover the real time dynamics of the system.

## 5 Evaluation of exchange parameters in disordered systems

The exchange parameters entering the Heisenberg model (1) can be estimated from first-principles using the magnetic force theorem as it is implemented within the multiple-scattering theory. For an ordered system the  $J$ 's can be determined as shown in [34]

$$J_{ij} = \frac{1}{4\pi} \int_{-\varepsilon_F}^{\varepsilon_F} d\varepsilon \text{Im} \text{Tr}_L \left[ \Delta_i(\varepsilon) G_{\downarrow}^{ij}(\varepsilon) \Delta_j(\varepsilon) G_{\uparrow}^{ji}(\varepsilon) \right], \quad (45)$$

where  $\text{Tr}_L$  denotes the trace over the angular momentum, and it is integrated up to the Fermi energy  $\varepsilon_F$ .  $G_{\sigma}^{ij}(\varepsilon)$  is the back scattering operator of a spin  $\sigma$  between the sites  $i$  and  $j$ , and  $\Delta_i(\varepsilon) = t_{\uparrow}^i(\varepsilon) - t_{\downarrow}^i(\varepsilon)$  is defined via the single scattering  $t$  matrices  $t_{\sigma}^i(\varepsilon)$  and closely related to the exchange splitting corresponding to the magnetic atom  $i$ . The Green function entering the

Eq. (45) can be calculated self-consistently using any implementation of the multiple scattering Green function method within the density functional theory [66, 67, 68, 69].

The magnetic force theorem (45) can be generalized for disordered systems using the coherent-potential approximation [70, 71]

$$J_{ij}^{\alpha\beta} = \frac{1}{4\pi} \int^{\epsilon_F} d\epsilon \text{Im} \text{Tr}_L \left[ \Delta_i^\alpha(\epsilon) (D_i^\alpha(\epsilon))^\dagger G_{\downarrow}^{ij}(\epsilon) D_j^\beta(\epsilon) \Delta_j^\beta(\epsilon) (D_j^\beta(\epsilon))^\dagger G^{ji\uparrow}(\epsilon) D_i^\alpha(\epsilon) \right], \quad (46)$$

where Greek letters denote atomic types and  $D_i^\alpha(\epsilon)$  is the so-called impurity matrix corresponding to an impurity atom  $\alpha$  on the site  $j$  [68]. The Green function in (46) is calculated self-consistently in a coherent medium  $t_c(\epsilon)$  and Fourier transformed into the real space.

## 6 The performance of the CPA scheme on the example of FeCo alloy

It is reasonable to inquire how an essentially mean-field-like CPA (Sec. 4) performs compared to the supercell simulations (Sec. 3), i.e., a numerically exact scheme. The question has been already answered for dilute magnets, i.e., uncorrelated mixtures of magnetic and non-magnetic atoms, in [57]. In short, the CPA provides an excellent account of the spin wave spectra in the high-dimensional structures above the percolation threshold.

Here, we ask the same question for mixtures of only magnetic atoms and answer it based on the example of bulk  $\text{Fe}_x\text{Co}_{1-x}$  alloys. We assume the uncorrelated disorder, i.e., an Fe atom is replaced with a probability  $1 - x$  on a parent bcc lattice by a Co atom, irrespective of the occupation of other sites around. The electronic ground state of the system, including the magnetic moments and the exchange constants  $J$ 's, is determined from the density functional theory. The details concerning the calculations of the exchange constants are given in Sec. 5.

The spin-wave spectrum of pure bcc-Fe has been thoroughly studied, cf. [47] and references therein. The dispersing spin waves form a single band. The energy of the least energetic magnon is zero, it is a Goldstone mode.

An introduction of Co to the parent lattice changes the magnetic system profoundly. The exchange interaction generally increase, become shorter-ranged, and loose their tendency to anti-ferromagnetic coupling between further shells. In general, this results in a broader magnonic bandwidth and less non-monotonic dispersion relation compared to the pure bcc-Fe. Another important feature is the appearance of a new class of weakly dispersive magnonic states. For weakly Co-doped alloys ( $x = 0.9$ ), these states appear above the continuum of acoustic magnons at around 700 meV (see Fig. 14). They are clearly discernible for large wave-vectors. The analysis of the corresponding magnonic modes in the real space clearly shows that these new states are strongly localized on the Co impurities while the modes in the acoustic continuum are generally delocalized and supported on the host Fe atoms. It should be remarked that such analysis is straightforward in the case of supercell calculations.

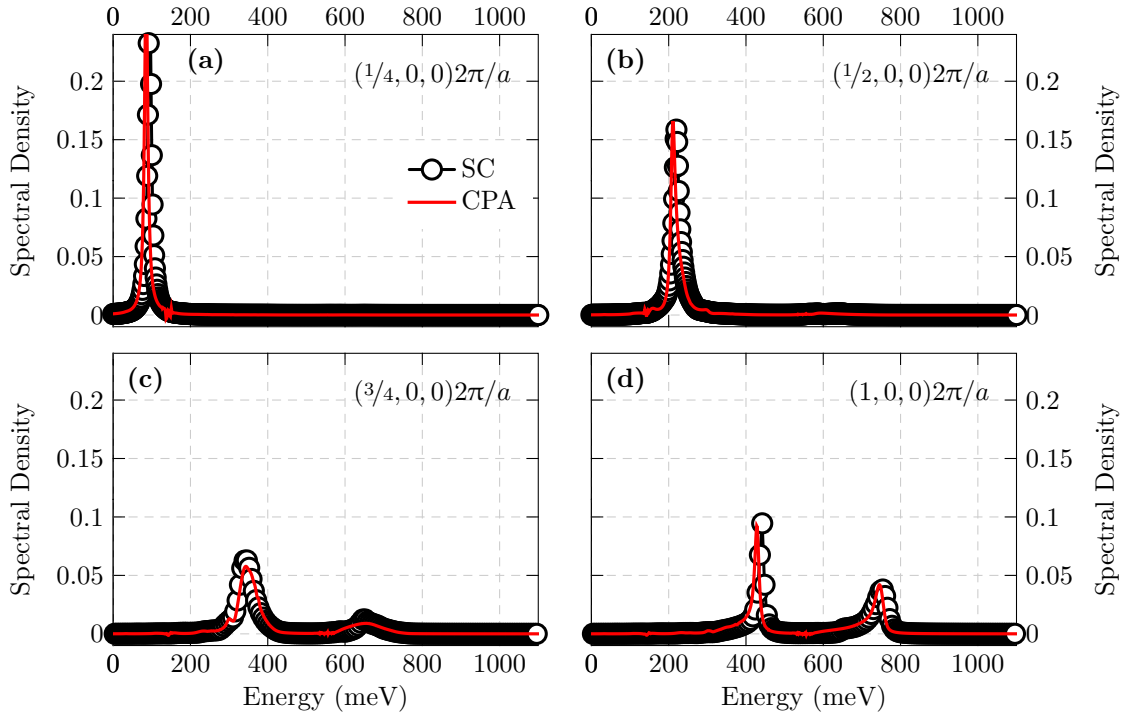


Figure 14: Magnonic spectrum of the  $\text{Fe}_{0.9}\text{Co}_{0.1}$  alloy for different wave vectors along (100) direction. The spectra obtained both using the CPA (red lines) and supercell (SC) schemes (black spheres) are presented.

The energy of these weakly dispersive magnon states gradually decreases with the increasing Co concentration. Around  $x = 0.8$  the states appear within the dispersing acoustic band, close to its top (not shown). Around  $x = 0.5$  they are located in the middle of the band at around 450 meV (see Fig. 15). We can clearly observe how for  $\mathbf{q} = (1/2, 0, 0)2\pi/a$  the more intense dispersing magnon state hybridizes with the weakly dispersing mode (see Fig. 15(b)). Because of this hybridization the magnonic state associated with the weakly dispersing mode is far less localized for large Co concentrations than its counterpart above the acoustic band for small Co concentrations.

Another interesting observation is the non-monotonous dependence of the acoustic spin wave peak's width on the state's energy. Low energy magnons with small momenta and the states close to the top of the dispersing band are associated with relatively narrow spectral peaks, i.e. they are long living. On the contrary, the magnons with the intermediate momenta, appearing in the middle of the band, correspond to wider peaks signifying stronger damping.

It is gratifying to observe that the CPA performs surprisingly well despite its mean field character. It is able to capture not only the emergence of the dispersing acoustic spin wave modes but also the weakly dispersive magnonic features both above (for low impurity concentration) and within (for high impurity concentration) the acoustic band. Furthermore, the CPA predicts correctly the energies and widths of all these magnon modes across the whole concentration range of Co impurities.

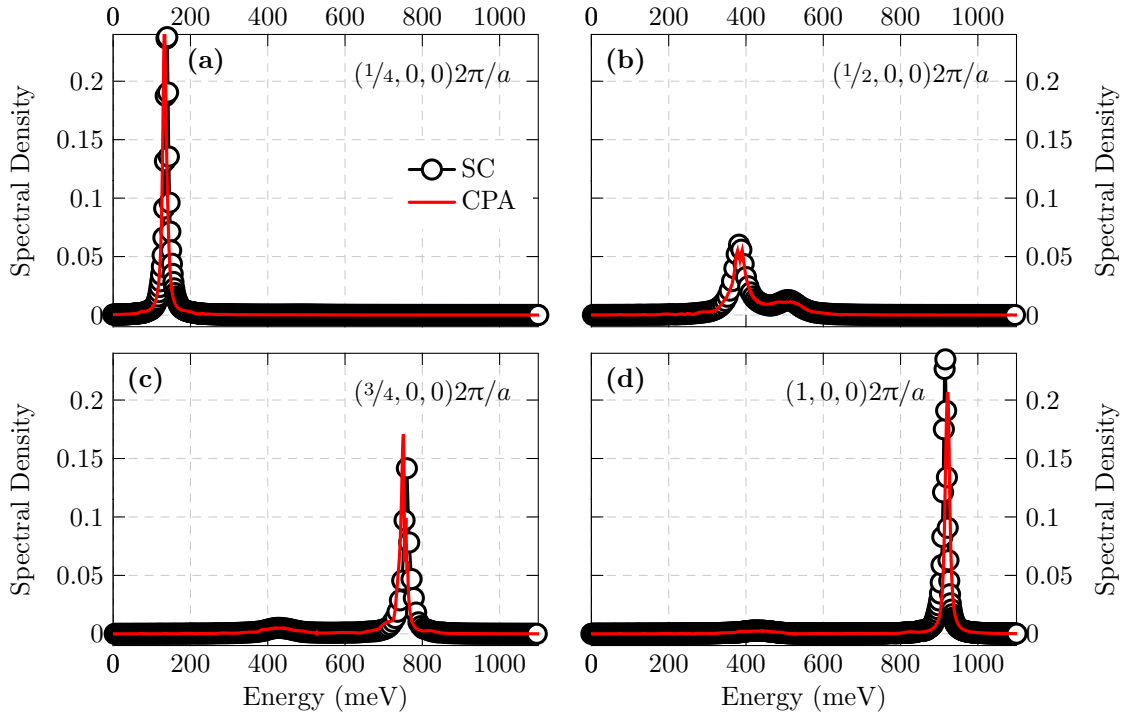


Figure 15: Magnonic spectrum of the  $\text{Fe}_{0.5}\text{Co}_{0.5}$  alloy for different wave vectors along (100) direction. The spectra obtained both using the CPA (red lines) and supercell (SC) schemes (black spheres) are presented.

## 7 Summary

In this Highlight, we presented our approach to determine the magnon properties in complex disordered magnetic systems. Our approach is based on the adiabatic mapping of a spin system on the Heisenberg Hamiltonian whereas the exchange integrals are computed from the *ab initio* density functional ground state. The disorder is treated with two complementary strategies. In the case of *uncorrelated* disorder one can resort to the CPA which we systematically derived here for the Heisenberg model. It is shown that the approximation performs surprisingly well despite its mean field character. The other strategy is the direct numerical simulation of large supercells using configurational average over possible samples. This approach is computationally much more demanding (contrary to the semi-analytic CPA calculations) but allows to study systems featuring *correlated* disorder effects, including clustering and formation of islands in two-dimensional systems, two effects very common in real magnets. It is shown that the inclusion of these effects is indispensable to the reliable theoretical interpretation of experimental results.

## Acknowledgements

This work was funded by *Deutsche Forschungsgemeinschaft* (DFG) within SFB 762. Kh. Z. acknowledges the support by the DFG through the Heisenberg Program ZA 902/3-1 and the

DFG Grant No. ZA 902/4-1. We are grateful to L. M. Sandratskii, T. Balashov, W. Wulhekel, and H. Ibach for fruitful discussions.

## References

- [1] F. Bloch. Zur Theorie des Ferromagnetismus. *Z. Physik*, 61:206, 1930.
- [2] T. Holstein and H. Primakoff. Field Dependence of the Intrinsic Domain Magnetization of a Ferromagnet. *Phys. Rev.*, 58:1098, 1940.
- [3] N. Majlis. *The Quantum Theory of Magnetism*. World Scientific, 2000.
- [4] Kh. Zakeri. Elementary spin excitations in ultrathin itinerant magnets. *Phys. Rep.*, 545:47, 2014.
- [5] S. V. Tyablikov. *Methods of Quantum Theory of Magnetism*. Plenum Press, New York, 1967.
- [6] Andrei Kirilyuk, Alexey V. Kimel, and Theo Rasing. Ultrafast optical manipulation of magnetic order. *Rev. Mod. Phys.*, 82:2731, 2010.
- [7] H. S. D. Cole and R. E. Turner. Magnon Enhancement of Electronic Specific Heat. *Phys. Rev. Lett.*, 19:501, 1967.
- [8] Marius V. Costache, German Bridoux, Ingmar Neumann, and Sergio O. Valenzuela. Magnon-drag thermopile. *Nat. Mater.*, 11:199, 2011.
- [9] J. P. Liu, E. Fullerton, O. Gutfleisch, and D. J. Sellmyer. *Nanoscale Magnetic Materials and Applications*. Springer. Berlin, Heidelberg, 2009.
- [10] Y. Onose, T. Ideue, H. Katsura, Y. Shiomi, N. Nagaosa, and Y. Tokura. Observation of the Magnon Hall Effect. *Science*, 329:297, 2010.
- [11] L. P. Levy and S. Lyle. *Magnetism and Superconductivity*. Springer. Berlin, Heidelberg, 2000.
- [12] Roy B. Woolsey and Robert M. White. Electron-Magnon Interaction in Ferromagnetic Semiconductors. *Phys. Rev. B*, 1:4474, 1970.
- [13] F. Essenberger, P. Buczek, A. Ernst, L. Sandratskii, and E. K. U. Gross. Paramagnons in FeSe close to a magnetic quantum phase transition: Ab initio study. *Phys. Rev. B*, 86:060412, 2012.
- [14] F. Essenberger, A. Sanna, P. Buczek, A. Ernst, L. Sandratskii, and E. K. U. Gross. Ab initio theory of iron-based superconductors. *Phys. Rev. B*, 94:014503, 2016.
- [15] G. Shirane, S. M. Shapiro, and J. M. Tranquada. *Neutron Scattering with a Triple-Axis Spectrometer: Basic Techniques*. Cambridge: Cambridge University Press, 2002.

- [16] T. Chatterji. *Neutron Scattering from Magnetic Materials*. Amsterdam: Elsevier, 2005.
- [17] P. A. Grünberg. Light scattering from magnetic surface excitations. *Prog. Surf. Sci.*, 18:1, 1985.
- [18] B. Hillebrands, P. Baumgart, and G. Güntherodt. Brillouin light scattering from spin waves in magnetic layers and multilayers. *Appl. Phys. A*, 49:589, 1989.
- [19] T. Balashov, A. F. Takács, W. Wulfhekel, and J. Kirschner. Magnon Excitation with Spin-Polarized Scanning Tunneling Microscopy. *Phys. Rev. Lett.*, 97:187201, 2006.
- [20] T. Balashov, A. F. Takács, M. Däne, A. Ernst, P. Bruno, and W. Wulfhekel. Inelastic electron-magnon interaction and spin transfer torque. *Phys. Rev. B*, 78:174404, 2008.
- [21] C. L. Gao, A. Ernst, G. Fischer, W. Hergert, P. Bruno, W. Wulfhekel, and J. Kirschner. Spin Wave Dispersion on the Nanometer Scale. *Phys. Rev. Lett.*, 101:167201, 2008.
- [22] T. Balashov, P. Buczek, L. Sandratskii, A. Ernst, and W. Wulfhekel. Magnon dispersion in thin magnetic films. *J. Phys.: Condens. Matter*, 26:394007, 2014.
- [23] G. T. Rado and J. R. Weertman. Spin-wave resonance in a ferromagnetic metal. *J. Phys. Chem. Solids*, 11:315, 1959.
- [24] M. Plihal, D. L. Mills, and J. Kirschner. Spin Wave Signature in the Spin Polarized Electron Energy Loss Spectrum of Ultrathin Fe Films: Theory and Experiment. *Phys. Rev. Lett.*, 82:2579, 1999.
- [25] R. Vollmer, M. Etzkorn, P. S. Anil Kumar, H. Ibach, and J. Kirschner. Spin-Polarized Electron Energy Loss Spectroscopy of High Energy, Large Wave Vector Spin Waves in Ultrathin fcc Co Films on Cu(001). *Phys. Rev. Lett.*, 91:147201, 2003.
- [26] M. Etzkorn, P.S. Anil Kumar, R. Vollmer, H. Ibach, and J. Kirschner. Spin waves in ultrathin Co-films measured by spin polarized electron energy loss spectroscopy. *Surf. Sci.*, 566-568:241, 2004.
- [27] J. Prokop, W. X. Tang, Y. Zhang, I. Tudosa, T. R. F. Peixoto, Kh. Zakeri, and J. Kirschner. Magnons in a Ferromagnetic Monolayer. *Phys. Rev. Lett.*, 102:177206, 2009.
- [28] Kh. Zakeri, Y. Zhang, J. Prokop, T.-H. Chuang, N. Sakr, W. X. Tang, and J. Kirschner. Asymmetric Spin-Wave Dispersion on Fe(110): Direct Evidence of the Dzyaloshinskii-Moriya Interaction. *Phys. Rev. Lett.*, 104:137203, 2010.
- [29] Kh. Zakeri, Y. Zhang, T.-H. Chuang, and J. Kirschner. Magnon Lifetimes on the Fe(110) Surface: The Role of Spin-Orbit Coupling. *Phys. Rev. Lett.*, 108:197205, 2012.
- [30] H. J. Qin, Kh. Zakeri, A. Ernst, T.-H. Chuang, Y.-J. Chen, Y. Meng, and J. Kirschner. Magnons in ultrathin ferromagnetic films with a large perpendicular magnetic anisotropy. *Phys. Rev. B*, 88:020404, 2013.

- [31] Y. Meng, Kh. Zakeri, A. Ernst, T.-H. Chuang, H. J. Qin, Y.-J. Chen, and J. Kirschner. Direct evidence of antiferromagnetic exchange interaction in Fe(001) films: Strong magnon softening at the high-symmetry  $\bar{M}$  point. *Phys. Rev. B*, 90:174437, 2014.
- [32] H. J. Qin, Kh. Zakeri, A. Ernst, L. M. Sandratskii, P. Buczek, A. Marmodoro, T. H. Chuang, Y. Zhang, and J. Kirschner. Long-living terahertz magnons in ultrathin metallic ferromagnets. *Nat. Commun.*, 6:6126, 2015.
- [33] Khalil Zakeri. Probing of the interfacial Heisenberg and Dzyaloshinskii–Moriya exchange interaction by magnon spectroscopy. *J. Phys.: Condens. Matter*, 29:013001, 2017.
- [34] A. I. Liechtenstein, M. I. Katsnelson, V. P. Antropov, and V. A. Gubanov. Local spin density functional approach to the theory of exchange interactions in ferromagnetic metals and alloys. *J. Magn. Magn. Mater.*, 67:65, 1987.
- [35] B. L. Gyorffy, A. J. Pindor, J. Staunton, G. M. Stocks, and H. Winter. A first-principles theory of ferromagnetic phase transitions in metals. *J. Phys. F: Met. Phys.*, 15:1337, 1985.
- [36] J. Staunton, B. L. Gyorffy, A. J. Pindor, G. M. Stocks, and H. Winter. Electronic structure of metallic ferromagnets above the Curie temperature. *J. Phys. F: Met. Phys.*, 15:1387, 1985.
- [37] L. M. Sandratskii. Noncollinear magnetism in itinerant-electron systems: theory and applications. *Adv. Phys.*, 47:91, 1998.
- [38] Erich Runge and E. K. U. Gross. Density-functional theory for time-dependent systems. *Phys. Rev. Lett.*, 52:997, 1984.
- [39] E. K. U. Gross and Walter K. Local density-functional theory of frequency-dependent linear response. *Phys. Rev. Lett.*, 55:2850, 1985.
- [40] E. Stenzel and H. Winter. A real-space method for the evaluation of the dynamic spin susceptibility of paramagnetic metals with application to palladium. *J. Phys. F: Met. Phys.*, 15:1571, 1985.
- [41] S. Y. Savrasov. A linearized direct approach for calculating the static response in solids. *Solid State Commun.*, 74:69, 1990.
- [42] S. Y. Savrasov. Linear Response Calculations of Spin Fluctuations. *Phys. Rev. Lett.*, 81:2570, 1998.
- [43] J. B. Staunton, J. Poulter, B. Ginatempo, E. Bruno, and D. D. Johnson. Spin fluctuations in nearly magnetic metals from ab initio dynamical spin susceptibility calculations: Application to Pd and  $Cr_{95}V_5$ . *Phys. Rev. B*, 62:1075, 2000.
- [44] O. Grotheer, C. Ederer, and M. Fähnle. Fast *ab initio* methods for the calculation of adiabatic spin wave spectra in complex systems. *Phys. Rev. B*, 63:100401, 2001.

- [45] P. Buczek, A. Ernst, P. Bruno, and L. M. Sandratskii. Energies and Lifetimes of Magnons in Complex Ferromagnets: A First-Principle Study of Heusler Alloys. *Phys. Rev. Lett.*, 102:247206, 2009.
- [46] Paweł Adam Buczek. *Spin dynamics of complex itinerant magnets*. PhD thesis, Martin Luther Universität Halle-Wittenberg, 2009.
- [47] P. Buczek, A. Ernst, and L. M. Sandratskii. Different dimensionality trends in the Landau damping of magnons in iron, cobalt, and nickel: Time-dependent density functional study. *Phys. Rev. B*, 84:174418, 2011.
- [48] S. Lounis, A. T. Costa, R. B. Muniz, and D. L. Mills. Theory of local dynamical magnetic susceptibilities from the Korringa-Kohn-Rostoker Green function method. *Phys. Rev. B*, 83:035109, 2011.
- [49] Paul Soven. Coherent-Potential Model of Substitutional Disordered Alloys. *Phys. Rev.*, 156:809, 1967.
- [50] B. L. Gyorffy. Coherent-Potential Approximation for a Nonoverlapping-Muffin-Tin-Potential Model of Random Substitutional Alloys. *Phys. Rev. B*, 5:2382, 1972.
- [51] Takeo Matsubara. An Application of CPA to a Random Spin System. *Progr. Theor. Phys. Suppl.*, 53:202, 1973.
- [52] A. Theumann. Generalized CPA approach to the disordered Heisenberg ferromagnet. *J. Phys. C*, 7:2328, 1974.
- [53] G. Bouzerar and P. Bruno. RPA-CPA theory for magnetism in disordered Heisenberg binary systems with long-range exchange integrals. *Phys. Rev. B*, 66:014410, 2002.
- [54] G. Bouzerar, J. Kudrnovský, L. Bergqvist, and P. Bruno. Ferromagnetism in diluted magnetic semiconductors: A comparison between *ab initio* mean-field, RPA, and Monte Carlo treatments. *Phys. Rev. B*, 68:081203, 2003.
- [55] Georges Bouzerar, Timothy Ziman, and Josef Kudrnovský. Compensation, interstitial defects, and ferromagnetism in diluted ferromagnetic semiconductors. *Phys. Rev. B*, 72:125207, 2005.
- [56] G. X. Tang and W. Nolting. Magnetic properties of disordered Heisenberg binary spin system with long-range exchange. *Phys. Rev. B*, 73:024415, 2006.
- [57] P. Buczek, L. M. Sandratskii, N. Buczek, S. Thomas, G. Vignale, and A. Ernst. Magnons in disordered nonstoichiometric low-dimensional magnets. *Phys. Rev. B*, 94:054407, 2016.
- [58] Timofey Balashov. *Inelastic scanning tunneling spectroscopy: magnetic excitations on the nanoscale*. PhD thesis, Universität Karlsruhe (TH), 2009.
- [59] Richard Durstenfeld. Algorithm 235: Random Permutation. *Commun. ACM*, 7:420, 1964.

- [60] Ken Perlin. An Image Synthesizer. *ACM SIGGRAPH Comp. Graph.*, 19:287, 1985.
- [61] Ken Perlin. Improving Noise. *ACM Trans. Graph.*, 21:681, 2002.
- [62] Kenneth Perlin. Standard for perlin noise, 2005. US Patent.
- [63] H. L. Meyerheim, R. Popescu, and J. Kirschner. No alloying in Fe deposited on Pd(001) at room temperature. *Phys. Rev. B*, 73:245432, 2006.
- [64] Fumiko Yonezawa and Kazuo Morigaki. Coherent Potential Approximation. Basic concepts and applications. *Progr. Theor. Phys. Suppl.*, 53:1, 1973.
- [65] J. A. Blackman, D. M. Esterling, and N. F. Berk. Generalized Locator Coherent-Potential Approach to Binary Alloys. *Phys. Rev. B*, 4:2412, 1971.
- [66] B. L. Gyorffy and M. J. Stott. *Theory of Soft X-Ray Emission from Alloys*, chapter Theory of Soft X-Ray Emission from Alloys, page 385. London and NY: Acad. Press, 1973.
- [67] M. Luders, A. Ernst, W. M. Temmerman, Z. Szotek, and P. J. Durham. Ab initio angle-resolved photoemission in multiple-scattering formulation. *J. Phys.: Condens. Matter*, 13:8587, 2001.
- [68] H. Ebert, D. Ködderitzsch, and J. Minár. Calculating condensed matter properties using the KKR-Green's function method: recent developments and applications. *Rep. Prog. Phys.*, 74:096501, 2011.
- [69] M. Geilhufe, S. Achilles, M. A. Köbis, M. Arnold, I Mertig, W. Hergert, and A. Ernst. Numerical solution of the relativistic single-site scattering problem for the Coulomb and the Mathieu potential. *J. Phys.: Condens. Matter*, 27:435202, 2015.
- [70] I. Turek, J. Kudrnovský, V. Drchal, P. Bruno, and S. Blügel. Ab initio theory of exchange interactions in itinerant magnets. *Phys. Status Solidi B*, 236:318, 2003.
- [71] I. Turek, J. Kudrnovský, V. Drchal, and P. Bruno. Exchange interactions, spin waves, and transition temperatures in itinerant magnets. *Philos. Mag.*, 86:1713, 2006.